SciMedCentral

Journal of
Radiology & Radiation
Therapy

Special Issue on
Head and Neck Imaging
Edited by:

Review Article

Quantification of Diffusion and Permeability of MRI in the Head and Neck Region

Toru Chikui[1]*, Masahiro Ohga[2], Erina Kitamoto[1], Tomoko Shiraishi[3], Shintaro Kawano[4], Takashi Yoshiura[5] and Kazunori Yoshiura[1]

[1]*Department of Oral and Maxillofacial Radiology, Kyushu University, Japan*
[2]*Department of Medical Technology, Kyushu University, Japan*
[3]*Department of Diagnostics and General Care, Fukuoka Dental College, Japan*
[4]*Section of Oral and Maxillofacial Oncology, Kyushu University, Japan*
[5]*Department of Clinical Radiology, Kyushu University, Japan*

***Corresponding author**
Toru Chikui, Department of Oral and Maxillofacial Radiology, Kyushu University 3-1-1 Maisahi, Higashi-ku, Fukuoka Japan, Tel: 81-92-6407; Fax: 81-92-6410; Email: chikui@rad.dent.kyushu-u.ac.jp

Submitted: 22 January 2014

Accepted: 28 February 2014

Published: 12 March 2014

ISSN: 2333-7095

Keywords
- Diffusion
- Permeability
- MRI
- Head and neck

Abstract

Diffusion Weighted Image (DWI) has various roles such as tissue characterization, the prediction and monitoring of the response to treatment and differentiation of recurrent tumors from post-therapeutic changes. The malignant tumors have a lower ADC compared to benign lesions. Follow-up of early response to cancer treatment is reflected in an ADC increase in the primary tumor and nodal metastases; whereas nonresponding lesions tend to reveal only a slight increase or even a decrease in ADC during follow-up. However, there are many limitations regarding the performance of DWI in the head and neck region, therefore, many attempts has been performed to overcome the flaws of the diffusion-weighted single-shot-echo planar imaging.

The pharmacokinetic analyses of dynamic contrast enhanced MRI (DCE-MRI) can provide physiological condition of the tissue, and Tofts and Kermode Model has been applied to the head and neck region. Some researchers have used it for the prediction and monitoring of the tumor response to cancer therapy. The general consensus is that the early changes of these parameters during the early phase after the treatment are useful for the interpretation of the response to the treatment. However, the parameters reported in the literature vary considerably; therefore, it is difficult to compare the values of the parameters among research groups.

Both DWI and the pharmacokinetic analysis of the DCE-MRI have shown a wide range of potential benefits in this region, but more comparative studies with established scan techniques and the quantification of the data are required.

ABBREVIATIONS

DWI: Diffusion-Weighted Image; DCE-MRI: Dynamic Contrast-Enhanced MRI; CM: Contrast Mediuwm; TIC; Time-Intensity Curve; WR: Washout Ratio; TK model: Tofts And Kermode Model; SI: Signal Intensity: Signal Intensity; MPG: Motion-Probing Gradient; ADC: Apparent Diffusion Coefficient; EPI: Echo Planar Imaging; SS-EPI: Single-Shot-Echo Planar Imaging; MS-EPI: Multi-Shot-Echo Planar Imaging; HASTE: Half-Fourier Single-Shot Turbo Spin-Echo; SPLICE: Split Acquisition of Fast Spin-

Cite this article: *Chikui T, Ohga M, Kitamoto E, Shiraishi T, Kawano S, et al. (2014) Quantification of Diffusion and Permeability of MRI in the Head and Neck Region. J Radiol Radiat Ther 2(2): 1047.*

Echo Signals; CRT: Chemoradiotherapy; RT: Radiotherapy; CR: Complete Response; PR: Partial Response, DTI: Diffusion Tensor Imaging; FA: Fractional Anisotropy; BV: Blood Volume; BF: Blood Flow; GRE-EPI: Gradient Echo Type EPI; EES: Extra vascular Extracellular Space; AIF: Arterial Input Function; SPGR: Spoiled Gradient Echo Sequence; UD: Undifferentiated; SCC: Squamous Cell Carcinoma; ML: Malignant Lymphoma; HNSCC: Head and Neck Squamous Cell Carcinoma; PG: Parotid Gland; FA: Flip Angle

INTRODUCTION

In Diffusion-Weighted MRI (DWI), the random microscopic motion of water protons determines the image contrast. Changes in proton self-diffusion are an early indicator of alterations in the cellular homeostasis in acute ischemic stroke; therefore, DWI has become an important tool for the early detection of ischemic stroke [1,2]. This technique is currently being evaluated for various extracranial lesions. Many limitations regarding the performance of extracranial DWI have recently been overcome, and it has various roles such as tissue characterization, the prediction and monitoring of the response to treatment and differentiation of recurrent tumors from post-therapeutic changes, such as fibrosis [3,4].

Dynamic Contrast-Enhanced MRI (DCE-MRI), in which multiphase scans are taken following the intravenous injection of a Contrast Medium (CM), has been widely used in clinical practice. The conventional assessment is the classification of the Time-Intensity Curve (TIC) regarding the time to peak enhancement (T_{peak}) and the Washout Ratio (WR). However, this does not provide information about the underlying pharmacokinetic parameters in the tissue. Conversely, the pharmacokinetic analyses can provide such information, and the most popular Tofts and Kermode Model (TK model) can provide information about the micro vessel permeability and the extracellular space [5-8]. A TK model analysis has been applied for the head and neck region, and some researchers have used it for the prediction and monitoring of the tumor response to cancer therapy.

The aim of this review is to present an overview of the principle, theory and clinical application of DWI and DCE-MRI for the head and neck region.

DWI

The principle of DWI: The most common approach to render MRI sensitive to diffusion is to use a spin echo pulse sequence, in which equal rectangular gradient pulses are played out before and after the 180°-refocusing pulse [9,10]. Without motion, the phase shift due to the two gradients will cancel out. If all spins move coherently (like stationary flow), all will acquire the same phase shift. However, if the spins move at random, the individual spins acquire various phase shifts, which leads to decreased Signal Intensity (SI) (Figure 1).

For simplicity, a Motion-Probing Gradient (MPG) is first applied to one direction belonging on the x-axis. The SI can be expressed as:

$$\ln\ln\left\{ {}^{S}\!/\!{}_{S_0} \right\} = -bD_{xx} \tag{1}$$

Where b is the diffusion sensitizing factors, and D_{xx} is the Apparent Diffusion Coefficient (ADC).

b can be expressed as:

$$b = \gamma^2 G^2 \delta^2 \left(\Delta - {}^{\delta}\!/\!{}_{3} \right) \tag{2}$$

here, γ is the gyromagnetic ratio, G is the strength of the gradient, δ is the duration of the one Motion Probing Gradient (MPG) lobe and Δ is the duration of time between the start of the MPG and that of the next MPG. By using multiple b values (at least two), we can obtain a D_{xx} value.

The diffusion time (τ_d) is determined as:

$$\tau_d = \left(\Delta - {}^{\delta}\!/\!{}_{3} \right) \tag{3}$$

The τ_d is considered to be the spent time for the material to diffuse during a pair of MPGs [9]. Note that as the diffusion time becomes larger *in vivo,* even if the b value is the same, the D_{xx} becomes smaller because barriers such as the cell membrane and sub cellular organelles restrict the diffusion of the water proton.

The diffusion coefficient can be calculated from eq. (1) by using multiple b values (at least two). The SI of DWI changes based on the direction of the MPG, and this phenomenon is called anisotropic diffusion [10]. It is well known that both the nerve and muscle fibers show anisotropic diffusion. However, in clinical practice, the isotropic DWI, which excludes the anisotropic aspect, is commonly used for other organs and tissues.

The most popular method employs MPGs that are applied along three directions (like x-, y- and z-axes) in order to obtain three DWIs. The SIs of these directions are multiplied to calculate the third root to obtain the isotropic DWI.

$$ADC = -\frac{\ln\ln\left\{ \sqrt[3]{SI_x SI_y SI_z} \,/\, SI_0 \right\}}{b} = \left(D_{xx} + D_{yy} + D_{zz} \right) / 3 \tag{4}$$

Another method involves the simultaneous application of MPGs with three directions and the combination of the changes in the polarity of the MPGs [12].

Technical limitations of DWI in the maxillofacial region: In clinical practice, diffusion-weighted Single-Shot-Echo Planar Imaging (SS-EPI) is commonly used, in which all data points necessary for the reconstruction of an image are sampled after a 90-180° RF pulse combination at a time [9]. The most critical point that must be kept in mind when performing DWI is to prevent the effects of macroscopic motion, like unwanted body motion, pulsing motion and so on, while retaining the information about the microscopic motion. This is the reason why SS-EPI, which is a type of ultrafast imaging, has been commonly used.

However, DW-SS-EPI has several flaws, which are especially prominent when used in the maxillofacial region [3,4,10]. These mainly consist of the problems derived from SS-EPI itself or those due to the strong Motion Probing-Gradient magnetic fields (MPGs).

EPI has a very small bandwidth per pixel in the phase encoding direction; therefore, EPI is very sensitive to causes of off-resonance, such as local susceptibility variation due to a dental prosthesis and the pneumatic space. The accumulated phase errors may induce image distortion. To compensate for the low bandwidth per pixel, SS-EPI has been combined with parallel imaging techniques. It reduces the amount of k-space data with an array of receiver coils. It increases the intervals of the lines of data acquisition in the k-space; therefore, it results in increased bandwidth in the phase-encoding direction. Moreover, it can shorten the echo time (TE), thereby diminishing the T2*-filtering [10].

Multishot-Echo-Planar Imaging (MS-EPI) is known to provide high resolution DWI with reduced geometric distortions compared to SS-EPI. The data acquisition can be divided into a number of shots with interleaved k-space trajectories, which reduces the image distortion. The navigator echo has been used to monitor the motion-induced phase shifts between each interleaf and to correct them. Moreover, cardiac gating or a pulse trigger can be used to reduce the effect of the pulsation [10-14]. Yamashita applied MS-EPI to the temporal bone, and demonstrated that MS-EPI was associated with higher sensitivity and accuracy than SS-EPI for the detection of cholesteatoma [15].

The steeply ramped gradient fields may generate significant eddy currents during their rapid on/off transition. If the eddy currents have not decayed during image readout, the residual magnetic field will be misread, and this will result in various distortions like scaling, parallel translation and shear deformation. Eddy current-related distortions are exacerbated in EPI due to the low bandwidth in the phase encoding.

Recently, the modification of the gradient pulse sequence by inserting additional gradients of opposite polarity has been applied so that the effects of individual eddy current are counterbalanced. The most widely implemented modification in clinical EPI-DWI is the twice-refocused spin-echo preparation (bipolar) [16]. Kyriazi demonstrated that artifact reduction makes the bipolar DWI sequence preferable for abdominopelvic applications [17]. To the best of our knowledge, there have been no reports of bipolar DWI in the head and neck region; however, this technique will like be used in this area due to its advantages over other techniques.

Despite the improvement of the image quality by using a combination of the EPI and parallel imaging techniques, image degeneration is still sometimes problematic. Hence, other (non-EPI) techniques which are insensitive to artifacts, such as half-Fourier single-shot turbo spin-echo (HASTE), the split acquisition of fast spin-echo signals (SPLICE) and diffusion-weighted line scan imaging, have been applied for the maxillofacial region [18-21].

Sakamoto evaluated 46 lesions and demonstrated that HASTE DWI is useful for predicting the malignancy of head and neck lesions [19]. Verhappen demonstrated that EPI-DWI has geometric distortions, which resulted in a lower interobserver agreement of ADCs of lesions than HASTE-DWI [18]. On the other hand, they also demonstrated that the lesions were more easily visualized on EPI-DWI compared with HASTE-DWI, due to the lower SNR of the latter sequence [18].

SPLICE is a modified technique using single-shot fast spin echo, which combines diffusion-sensitive stimulated-echo preparation and split-echo acquisition. Sakamoto applied this technique to 67 head and neck lesions, and demonstrated that no cases showed severe image distortion on DWI with SPLICE, and reliable ADC maps were obtained in all cases [20]. Yoshino also demonstrated the utility of SPLICE for evaluating salivary gland lesions [21].

A sophisticated method that combines fast spin-echo and radial scanning has been proposed, and has commonly been known as PROLLELER, or BLADE. In one TR, the data are acquired within a rectangle-shaped blade in parallel lines of the k-space. In the subsequent TRs, the blade is rotated centered at the origin to measure the remaining parts of the k-space. The oversampled data at the center of the k-space are used to correct the inconsistencies between the data from each blade [22,23].

Clinical application of DWI for the maxillofacial region: One of the first successful DWI investigations to be performed in the head and neck region showed the potential for distinguishing solid from cystic lesions, and the general results showed that the mean ADC value of benign solid tumors is higher than that of malign tumors [24,25].

Many researchers have confirmed that ADC is an important tool for the differential diagnosis of salivary gland tumors. Warthin's tumors include polyclonal lymphocytes with conspicuous follicles and a germinal center, which resulted in low ADC values. On the other hand, pleomorphic adenoma has a rich stromal composition like myxomatous tissue, which results in higher ADC values. A final distinction between Warthin's tumors and malignant tumors is difficult, owing to the overlapping of the ADC values of the two categories [26-29]. Therefore, Yabuuchi proved the value of combining the results from DWI and DCE-MRI [29].

DWI has been applied for the differential diagnosis of metastatic and reactive nodes [30-35]. The general consensus is that metastatic lymph nodes consistently have a significantly lower ADC compared to benign lymph nodes. The densely packed enlarged cells and increased mitotic figures may act as a barrier to the diffusion of water molecules. On the contrary, Sumi demonstrated that a higher ADC suggested the high possibility of metastasis [33]. The contradictory results may be related to the ratio of the necrotic areas in the regions of interest examined. Zhange et al. demonstrated the importance of the separation of necrotic and solid portions, and the ADC values of these portions are useful in differentiating between the causes of cervical lymphadenopathy [34], Moreover, Park et al. performed high resolution DWI and suggested that the ADC of the lymph node was dependent on whether the hilum was included in the region of interest [35]. Therefore, further studies of the DWI with high spatial resolution will be needed.

Many researchers have discussed both the prediction and monitoring of the tumor response to cancer therapy [36-44]. Hatakenaka evaluated 38 patients with head and neck squamous cell carcinoma (HNSCC) treated by Chemoradiotherapy (CRT) or Radiotherapy (RT) with a radiation dose to the gross tumor volume of more than 60 Gy. They demonstrated that a higher pretreatment ADC value suggested a higher possibility of local recurrence [36]. Onishi evaluated 64 consecutive patients with SCC of the hypopharynx or oropharynx treated with definitive RT, and demonstrated a high ratio of local control in the tumors with lower ADC values [37]. However, either Vandecaveye or

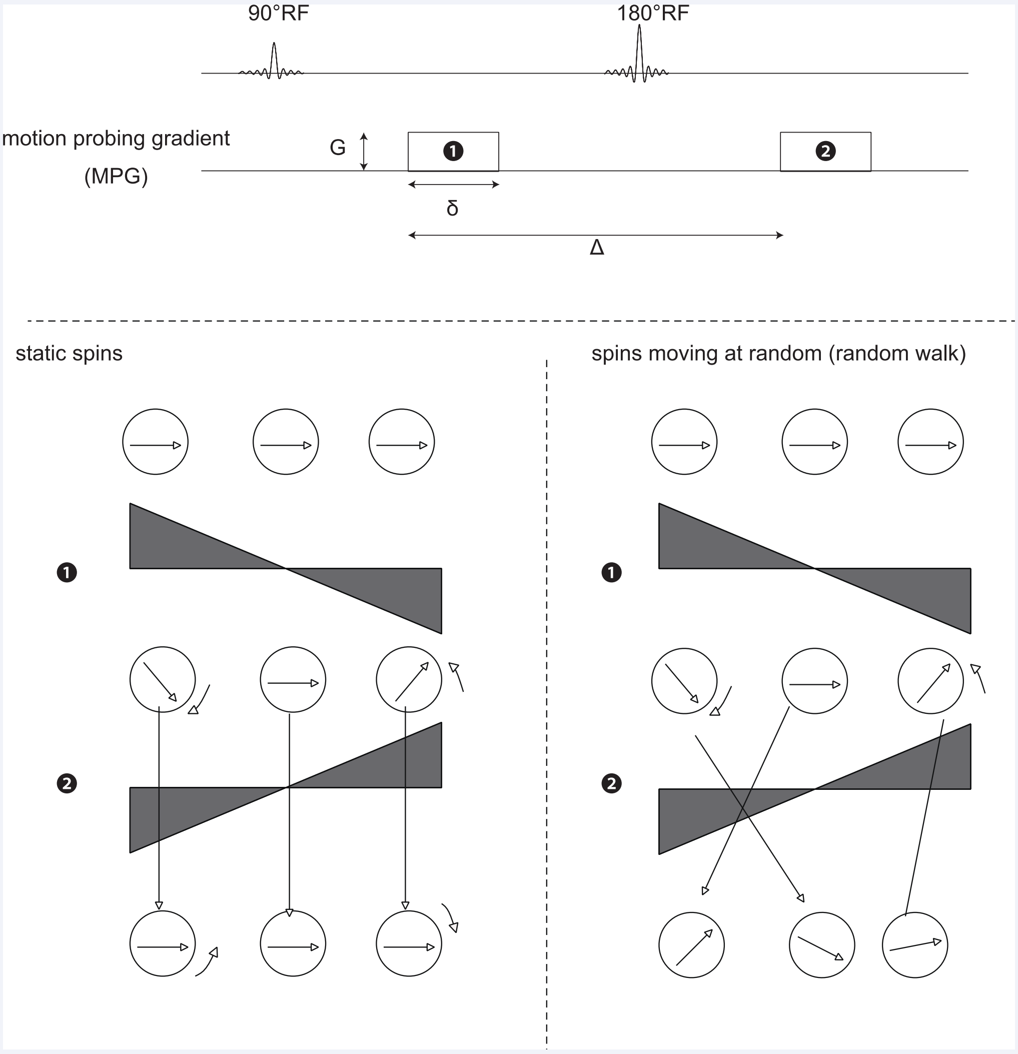

Figure 1 A schematic illustration of DWI. The upper line shows the motion-probing gradient (MPG). Equal rectangular gradient pulses are played out before and after the 180°-refocusing pulse (upper). Without motion, the phase shift due the two gradients will cancel out (lower left). If the spins move at random, the individual spins acquire various phase shifts, which leads to a decrease of the signal intensity (lower right). G: Diffusion-weighted gradients of strength, δ: duration Δ: spacing.

King[40-42] could not corroborate these results in the studies. Therefore, the usefulness of the pre-treatment ADC for predicting the response to cancer therapy is controversial.

On the other hand, many researchers have supported that the increase in the ADC during the early phase after the treatment (or during the treatment) is associated with a good response to the treatment [38,41-44]. The tumor ADC increases after initiating treatment because of cellular damage leading to tumor lysis, a loss of cell membrane integrity and apoptosis. Although tissue responses like fibrosis and fat infiltration also modify the ADC, the ADC increase can be observed in response to a range of cancer therapies within one to two months in many cancers. A study of 33 patients with cervical lymph node metastases from SCC showed a significantly higher increase in the mean ADC one week after the start of combined chemo- and radiation therapy in the Complete Response (CR) group compared with that in the partial response (PR) group [41]. Similar results were obtained in a study in which 30 patients treated by CRT for HNSCC underwent MRI exams before and at two and four weeks after starting treatment. The two-year locoregional control rate was significantly higher for the tumors with larger ADC increases between the pre-treatment and early post-treatment measurements [42].

We performed DWI exams with b factors of 0, 500, 1,000 and 1,500 s/mm^2 before and after preoperative CRT (n = 37). The histological evaluation of the effects of CRT was performed according to Ohboshi and Shimosato's classification in the excised specimen after surgery. These criteria grade the tumor response from I (minimal change) to IV (complete disappearance of the tumor cells) [45]. Patients with grades IIb, III and IV responses are considered to be responders, while those with grades IIa and I responses are considered to be non-responders. There was no significant difference between the pre-treatment ADC of the responders [(1.11±0.11) x 10^{-3}mm^2/s] and that of the non-responders [(1.06±0.07) x 10^{-3}mm^2/s] (P=0.189). However, the post-treatment ADC of the responders [(1.36±0.15)x 10^{-3}mm^2/s] was significantly higher than that of non-responders [(1.21±0.21) x 10^{-3}mm^2/s] (P=0.047) (Figure 2).

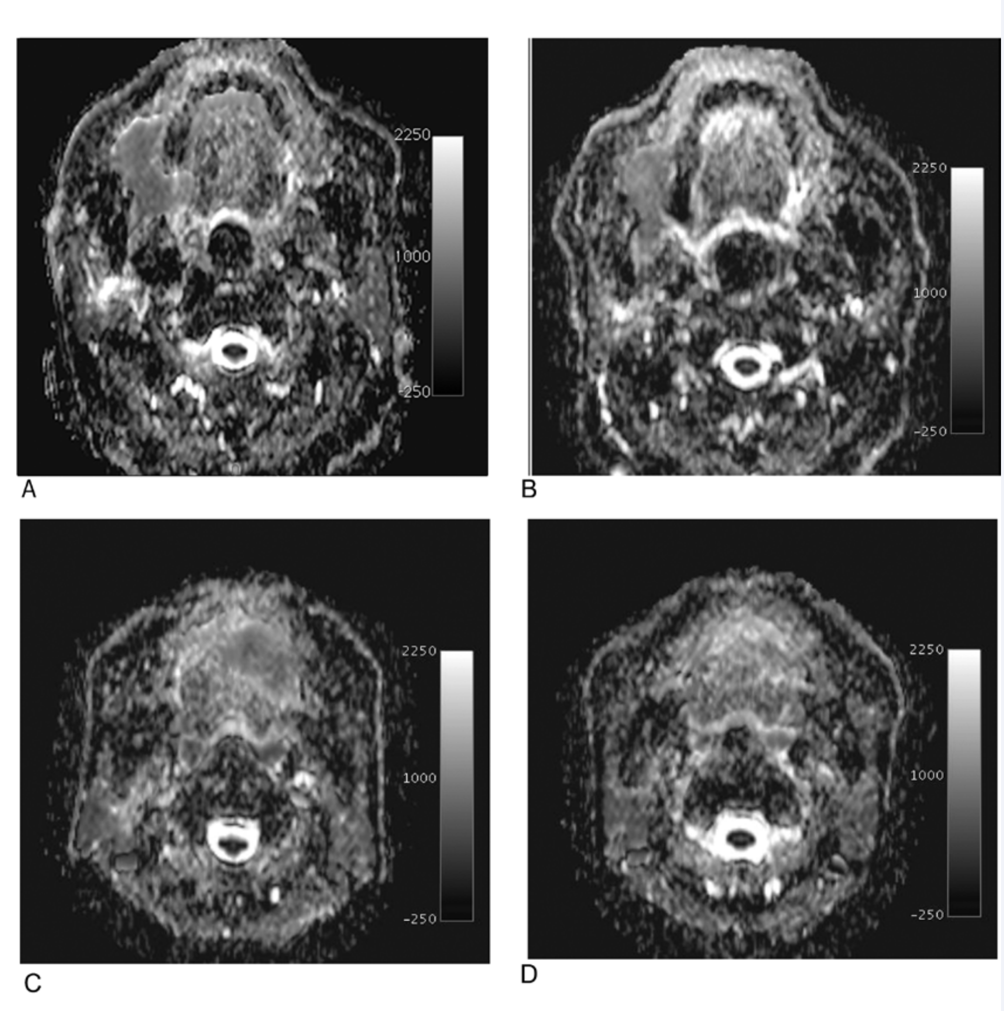

Figure 2 A non-responder with an Ohboshi and Shimosato classification of I (a, b). The pre-treatment ADC was 1.07x10^{-3} mm^{2}/s and the post-treatment ADC was 1.07x10^{-3} mm^{2}/s, therefore the change was small. A responder with an Ohboshi and Shimosato classification of III (c, d). The pre-treatment ADC was 1.06x10^{-3} mm^{2}/s and the post-treatment ADC was 1.33x10^{-3}mm^{2}/s, therefore, the change was large.

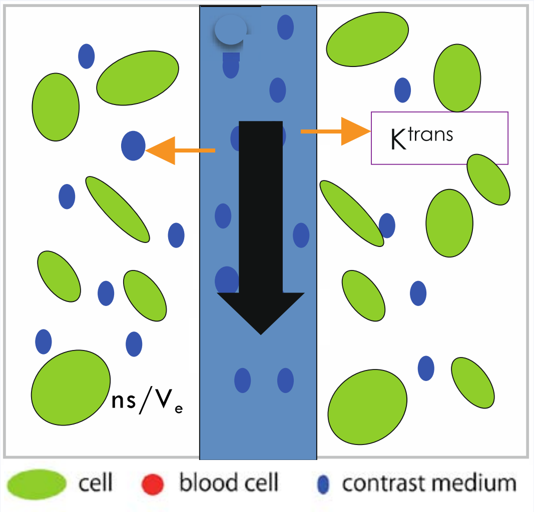

Figure 3 A schematic illustration of the TK model. The model assumes an equilibrium of the contrast media between the plasma and the extravascular-extracellular space (EES) and the isodirectional permeability. K^{trans}: the influx forward volume transfer constant (into the EES from the plasma), ve: the fractional volume of EES per unit volume of tissue, Kep: the efflux rate constant from the EES to plasma (K$_{ep}$ = K^{trans}/ve).

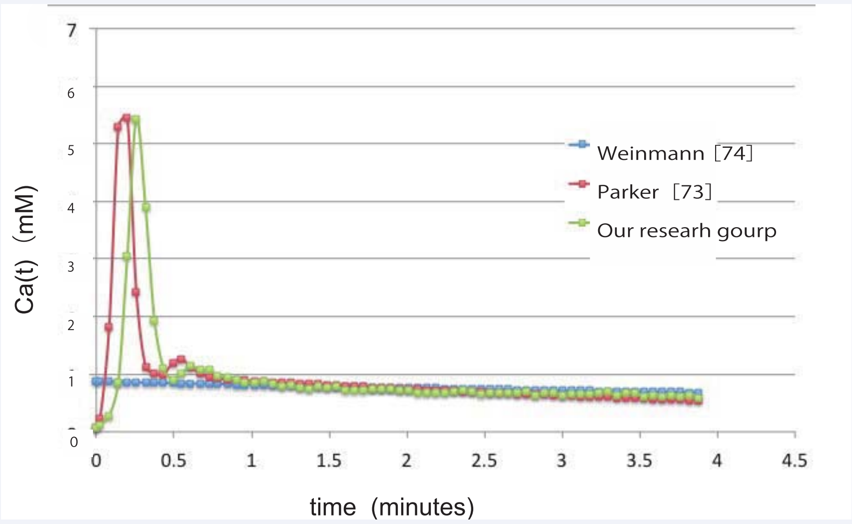

Figure 4 A comparison of the population-based AIF derived from the work by Weinmann (drip infusion), Parkers (injection rate: 3 ml/s, temporal resolution of DCE-MRI: 4.97s) and our group (2 ml/s, 3.5s). We used the phase images to obtain the C_a:

$\Delta\varphi = 2/3\ (TE\ \pi\gamma B_0\ \chi_m C_a)$

where γ is the proton gyromagnetic ratio, B_0 is the magnitude of the main magnetic field, χ_m is the molar susceptibility of the CM. We assumed that the direction of the carotid artery is parallel to that of the main magnetic field.

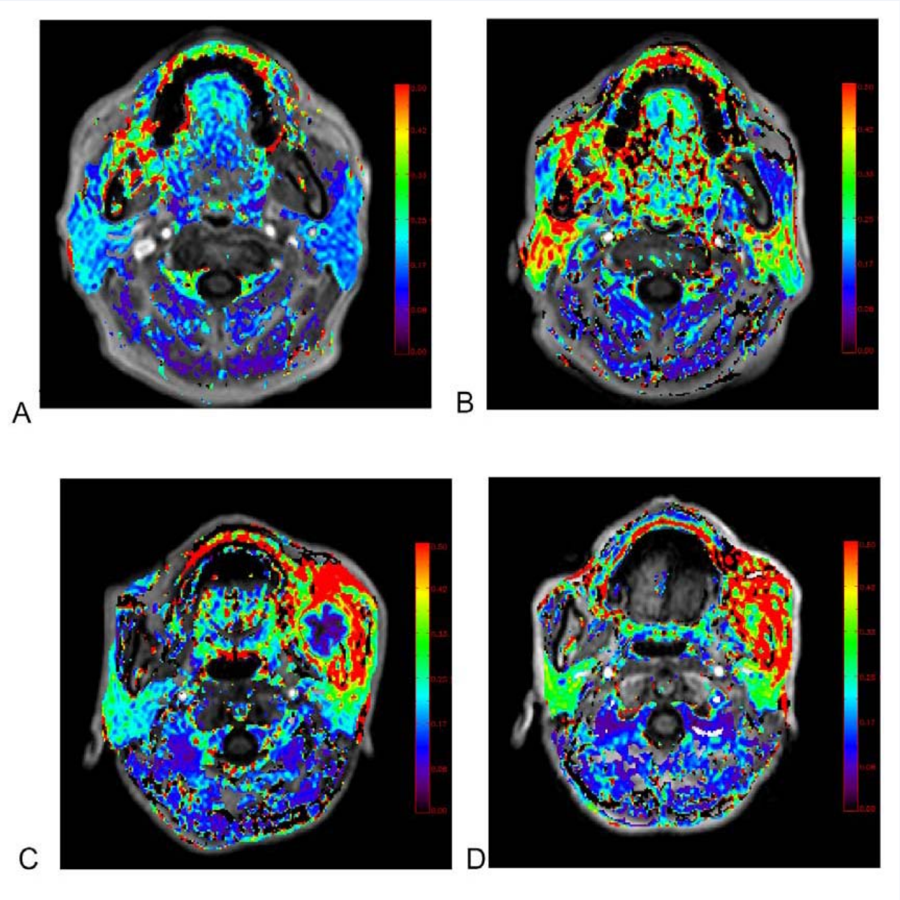

Figure 5 A 64-year-old male with SCC in the right lower gum. Non-responder with an Ohboshi and Shimosato classification of a (A, B). The pretreatment v_e was 0.37 (A) and the posttreatment v_e was 0.37 (B). The tumor ROI is drawn in red. A 61-year-old male with SCC in the left lower gum. Responder with Ohboshi and Shimosato classification of III (C, D). The pretreatment v_e was 0.25 and the posttreatment v_e was 0.46, therefore the change was large. The tumor ROI is drawn in red.

As discussed above, DW MRI can have a major impact on both the differential diagnosis and the monitoring of the tumor response to treatment. The choice of timing for follow-up studies is very difficult, because this decision depends on the tumor type and the methods of treatment [43].

The principle of diffusion tensor imaging (DTI), and its applications in the maxillofacial region: Considering the anisotropic nature of the tissue, a diffusion tensor

$$\overline{D} = \begin{pmatrix} D_{xx} & D_{xy} & D_{zx} \\ D_{xy} & D_{yy} & D_{yz} \\ D_{zx} & D_{yz} & D_{zz} \end{pmatrix} \tag{5}$$

is required to fully characterize the diffusion. $\overline{D}$ Could be obtained by using the following equation:

$$\ln\left(\frac{SI}{SI_0}\right) = -\gamma^2 \int_0^t \left[\int_0^{t'} \overline{G(t")}\, dt"\right] \bullet \overline{D} \bullet \left[\int_0^{t'} \overline{G(t")}\, dt"\right] \mathrm{dt'} \tag{6}$$

Where $\overline{G(t")}$ is the function of the gradient magnetic field. Equation (1) is the simplest special form of equation (6). MPGs in more than six directions are necessary for the estimation of $\overline{D}$ [11].

Most quantities of $\overline{D}$ are eigenvalues o (λ_1, λ_2 andλ_3, λ_1, $>\lambda_2>\lambda_3$) and three eigenvectors. Eigenvalues are the diffusion coefficients along the three intrinsic coordinated directions.

Several scalar parameters to represent the Diffusion Tensor (DT) have been proposed. Fractional anisotropy (FA) is a representative parameter, which shows the anisotropy, and can be determined as follows:

$$FA = \sqrt{\tfrac{1}{2}} \sqrt{\frac{(\lambda_1-\lambda_2)^2 + (\lambda_2-\lambda_3)^2 + (\lambda_3-\lambda_1)^2}{\lambda_1{}^2 + \lambda_2{}^2 + \lambda_3{}^2}} \tag{7}$$

In anisotropic tissues such as nerve fiber [46] and skeletal muscle [47], a 3D tissue fiber structure can be assessed with fiber tractography. The fiber tractographic analysis of DT MRI data is based on the assumption that the primary eigenvector of the DT coincide with the local fiber orientation.

There have been only a few reports of DTI and tractography in the maxillofacial region [48-51]. Hodaie evaluated five trigeminal neuralgia patients treated with Gamma Knife radiosurgery, which they found resulted in a 47% drop in FA values at the target [48]. By using tractography, Taoka described the facial nerve and evaluated the displacement of the facial nerve by a vestibular schwanomma in the cerebellopontine angle [49]. An attempt to depict the inferior alveolar nerve was also reported [50].

In muscle, the first eigenvalue represents the diffusion along the main direction of the muscle fiber, and the second and third eigenvalues represent the diffusion of water within the endomysium and throughout the fiber radius, respectively [52,53]. Shiraishi et al. applied DTI to the masseter muscle and showed that the first eigenvalue (λ_1) represents diffusion along the main direction of muscle. They also demonstrated that the eigenvalues for the diffusion of the masseter muscle were sensitive to the jaw position. The values of λ_2 and λ_3 during jaw opening were significantly lower than those at rest, and they considered that the phenomenon reflected a decrease in myofibril size and accompanying shrinkage of the endomysium [54,55].

These results are compatible with the results obtained from the extremities [56-58]. They considered that information provided by the DW and DT images has the potential to aid in the diagnosis of temporomandibular disorder (type I), hyperplasia of the tendon, and aponeuroses of the masticatory muscles.

However, these reports were all preliminary research studies. Therefore, the usefulness of DTI in the maxillofacial region will need to be evaluated in the future.

Dynamic contrast-enhanced MRI (DCE-MRI)

The theory of the quantification of DCE-MRI: Fundamentally, dynamic MR scans can be grouped into two categories; T_1-weighted DCE-MRI and T_2*-weighted DCE-MRI. The presence of CM within the vessel causes dephasing and shortens the T_2* value. T_2*-weighted sequences are therefore used to monitor the passage of the CM, because there is a transient darkening of the tissue during the first passage of the CM. Generally, the quantification is performed based on the assumption that the CM is confined in the capillary bed, which provides valuable information about perfusion, such as the blood volume (BV), blood flow (BF) and transit time. Such imaging requires fast acquisition (i.e., sub second and a few seconds); therefore, the gradient echo type EPI (GRE-EPI) has been widely used to allow for greater anatomical coverage. In the normal brain, the CM is confined to the vessels due to the brain-blood barrier, so the change of the T_1 relaxation time surrounding the vessel is extremely small. However, the susceptibility effect (the shortening of the T2* relaxation time) covers a much wider range. This is one reason why T2*-weighted DCE-MRI is commonly used to evaluate the perfusion of the brain [59]. However, GRE-EPI has limited applications in extracranial tissues owing to the great intrinsic sensitivity of its susceptibility. The image quality is especially poor in the head and neck region because of the pneumatic space and the presence of oral prostheses.

On the other hand, the basic principal of T_1-weighted DCE-MRI is the shortening of the T_1 value, which results in an increase of the SI. The shortening effect of the T_1 relaxation time occurs when the paramagnetic ion approaches within 5 of a water proton. In most tissues, except the normal brain, the CM leaks into the extravascular Extracellular Space (EES), and this causes the shortening of the T_1 relaxation time. Hence, T_1-weighted DCE-MRI could be applied to almost all tissues, including the maxillofatiocal region.

A simple evaluation of T_1-weighted DCE-MRI is the subjective assessment of the pattern of the TIC or the simple quantification of the TIC, like the time to peak enhancement (T_{peak}) and the Washout Ratio (WR). Although the semiquantitative evaluations described above have been widely applied in the maxillofacial region[60-64], they do not provide information on the underlying pharmacokinetic nature of the tissue. A pharmacokinetic analysis can show the underlying physiological characteristics of the lesion. We will now introduce the methods used for the pharmacokinetic analysis, and also describe the clinical application of this technique.

Although various kinds of compartment models [7,65] have been suggested for the quantification of T_1-weighted DCE MRI, the TK model [5,6,66] has been the most widely applied for various tissues. The TK model assumes the equilibrium of contrast media between the plasma and the extravascular-extracellular space (EES), and the isodirectional permeability. Therefore, the equilibrium is described by:

$$\frac{dC_t}{dt} = K^{trans}\left(C_p - \frac{C_t}{v_e}\right) \qquad (8)$$

Where t is the time, C_t is the CM in the tissue, C_p is the concentration of CM in plasma, K^{trans} is the influx forward volume transfer constant (into the EES from the plasma) and v_e is the fractional volume of the EES per unit volume of tissue (Figure 3).

In this model, the concentration of the CM is derived from the EES and plasma:

$$C_t(t) = K^{trans}\int_0^t C_p(t')\exp\left\{-\frac{K^{trans}(t-t')}{v_e}\right\}dt' + v_p C_p(t) \qquad (9)$$

Where v_e is the fractional volume of plasma per unit volume of tissue.

If the plasma component is negligible, the second term in the right part of the equation is eliminated. Substituting C_t (t) and C_p (t) into the equation allows the variables (K^{trans}, v_e, and v_p) to be estimated.

Although T_1-weighted DCE-MRI researchers have employed T_1-weighted gradient-echo, saturation recovery/inversion recovery snapshot sequences (e.g., turbo FLASH) [67] and EPI sequences, most studies have used the T_1-weighted gradient-echo (3D-transverse spoiled gradient echo sequence (SPGR)) in the maxillofacial region.

There are two steps required to estimate the concentration of CM. The first step is to obtain the pre-contrast T_1 map (T_{10} map). The relationship between the MR signal (SI) of a gradient echo and the relaxation time can be expressed as follows:

$$SI \propto \left[\left\{1-\exp\left(-TR/T_1\right)\right\}\exp\left(-TE/T_2{*}\right)\sin\sin\alpha \Big/ 1-\exp\left(-TR/T_1\right)\cos\cos\alpha\right] \qquad (10)$$

Where r is the proton density, α is the flip angle, TR is the repetition time, TE is the echo time and T_1 is the tissue T_1 value. By varying either the flip angle or the TR before the administration of CM, the T_{10} map can be obtained.

The second step is to obtain the T_1 map after the injection of CM using both the SI ratio (SI/SI_{pre}) and the T_{10} map. If the change in T_2* was assumed to be negligible due to full T_1 weighting, the SI ratio can be expressed as follows:

$$\frac{SI}{SI_{pre}} = \left\{\frac{1-\exp\left(TR/T_1\right)}{1-\exp\left(TR/T_{10}\right)}\right\}\left\{\frac{1-\exp\left(TR/T_{10}\right)\cos\cos\alpha}{1-\exp\left(TR/T_1\right)\cos\cos\alpha}\right\} \qquad (11).$$

The change of the relaxation rate ($1/T_1$) is parallel to the concentration of CM:

$$\frac{1}{T_1} = \frac{1}{T_{10}} + R_l C \qquad (12)$$

Where R_1 is a relaxation rate determined for each CM, and C is the concentration of CM during the dynamic sequence. These values substitute into the equation, and the variables (K^{trans}, v_e, and v_p) to be estimated.

The TK model analysis has several drawbacks based on the theory. The K^{trans} is determined by:

$$K^{trans} = F \bullet \rho \bullet (1-Hct)\left\{1-\exp\left(-\frac{PS}{F \bullet (1-Hct)}\right\} \qquad (13)$$

Where F is the blood flow, ρ is the specific gravity, Hct is the hematocrit and PS is the permeability-surface area product. Therefore, it is impossible to discriminate the effect of BF and that of permeability [68]. In addition, the premised instant mixing of CM between two compartments (EES and plasma) does not occur [7].

From the technical aspects, the applied Arterial Input Function (AIF) and the methods used for the T_1 measurements have a strong impact on these parameters. Although the estimation of the individual AIF is preferable [69], determining the AIF in the neck is challenging due to saturation due to the high concentration of CM and the inflow phenomenon due to the high velocity in the carotid artery. Recently, several attempted improvements of the scan method insensitive to flow (like turbo Flash) [67] and the utilization of phase images (phase AIF) [70-72] have been made. However, many researchers have used the model AIF based on the previous reports [73,74]. Figure 4 shows a comparison of the population-based AIF derived from the work by Weinmann (drip infusion), Parkers (injection rate: 3 ml/s, temporal resolution of DCE-MRI: 4.97s) and our group (2 ml/s, 3.5s). We used the phase images to obtain the C_a (t).

If the T_1 map was obtained by the SPGR method, the selection of the flip angles can lead to large differences in the T_1 value and the kinetic parameter estimation [75,76] Especially for 3T MRI, the inhomogeneity of the local magnetic field (B_1) has to be corrected, because the actual FA is quite different from the nominated FA [77,78]. Further research will be needed to perform a pharmacokinetic analysis.

Clinical application of the TK model analysis in the maxillofacial region: Lee et al. applied a pharmacokinetic analysis for 63 patients with 26 undifferentiated (UD) carcinomas, 28 squamous cell carcinoma (SCC) and eight malignant lymphomas (ML). They showed significant differences between UD/SCC and UD/lymphoma and suggested that their K^{trans} results appear to correlate with the expression of vascular endothelial growth factor. The v_e of the lymphoma was the smallest among the three types of tumors; however, the differences were not significant [79]. In our study, in which we evaluated 59 lesions, malignant lymphoma had the lowest v_e, and there were significant differences between malignant lymphoma and the other two malignant tumor types (SCC and malignant salivary gland tumor). Van Cann evaluated the mandibular invasion of SCC adjacent or fixed to the mandible (n=33), and demonstrated that SCC with medullary invasion showed a higher mean K^{trans} compared with SCC without invasion ($p < 0.001$) [80].

The pharmacokinetic analyses have been widely applied for the pre-treatment prediction of the therapeutic efficacy and for monitoring the tumor response to cancer therapies [81-88].

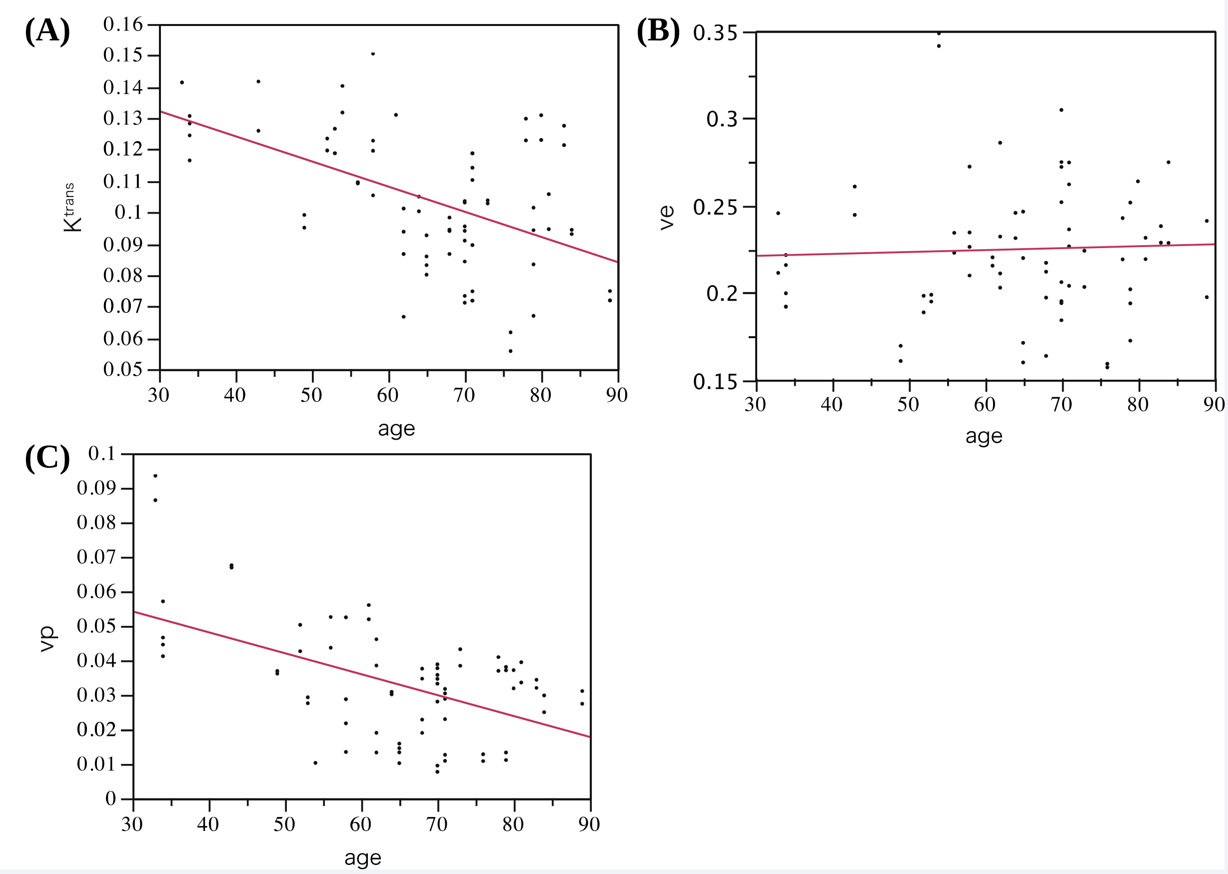

Figure 6 The correlations between the age and the parameters are shown. The age significantly and negatively correlated with the K^{trans} (P<0.0001; ρ= –0.513) (a) and v_p (P=0.0031; ρ= –0.499)(c), but not with the v_e (P=0.341)(b).

Several studies demonstrated that CRT is more effective against tumors with a higher pre-treatment K^{trans} than those with a lower K^{trans}, and suggested that the elevated BF and permeable vasculature had higher oxygenation levels, thus resulting in better access to the chemotherapeutic drug and better radio sensitivity. Kim et al. enrolled 33 HNSCC patients treated with neoadjuvant CRT. The treatment included accelerated RT with 220 cGy per fraction for a total dose of 70.4Gy. They demonstrated that the average pre-treatment K^{trans} of the CR group was significantly higher than that of the PR group [84]. Chawla et al. evaluated thirty-two patients with HNSCC who were treated by CRT; the radiation therapy regimen included a total dose of 70.4 Gy given in 32 fractions. They observed a higher K^{trans} value in responders compared with nonresponders; however, the difference was not significant [39]. Shukla-Dave et al. demonstrated that an increased pre-treatment skewness K^{trans} was associated with a poor overall survival and progression-free survival (n=74) [83].

Some HNSCC studies found that a large reduction of the permeability (K^{trans}) was linked to a better response to CRT [81,85]. However, with regard to the early changes in parameters, other studies demonstrated conflicting results, where an increase of permeability (K^{trans}) or the BV after CRT suggested a favorable outcome [82,86,87]. Cao et al. performed a quantification of the BV and BF based on DCE-MRI taken before treatment and two weeks after the initiation of CRT (n = 14). They also evaluated the local and regional control, and concluded that an increase of the BV and BF suggested a good outcome [82].

We performed DCE-MRI on patients with oral SCC before and after preoperative CRT (n = 29). The histological evaluation of the effects of CRT was performed according to Ohboshi and Shimosato's classification. The change in the K^{trans} of the responders was significantly larger than that of the non-responders (P = 0. 018) [86]. We considered that an increase in the available primary tumor blood supply for oxygen extraction during RT was associated with an increased tumor response. RT causes a significant increase in the EES, and moreover, the degree of tumor response is correlated with the increase in the EES (Figure 5) [86].

Outside of tumors, a TK model analysis has been applied to evaluate the function of the parotid gland (PG) [89-91]. We evaluated whether age had an effect on the parameters (K^{trans}, v_e, v_p and the volume of PGs) in 72 PGs. We found that age significantly and negatively correlated with the K^{trans} (P<0.0001; ρ= –0.513) and v_p (P=0.0031; ρ= –0.499), but not with either the v_e (P=0.341) or the volume of the PG (P=0.104) (Figure 6). It seems natural that the decrease in both the permeability of the vessels and the BF associated with aging resulted in a decrease in the K^{trans}. On the other hand, the age did not correlate with either the v_e or volume of the PGs. Many previous reports have demonstrated that the CT value decreased with age because of the deposition of fat. We considered that, in spite of the loss of the acinar cells with age, the deposition of fat prevented an increase in the v_e.

Roberts compared the microvascular characteristics of the parotid glands in patients with Sjögren syndrome with those in healthy volunteers. The distribution of the K^{trans}, and the v_e parameter values, were significantly different ($P< 0.001$) between the two subject groups, with group median parameters found to be elevated in the Sjögren syndrome group [89].

Houweling investigated radiation-induced changes in the salivary glands of patients with oropharynx cancer treated by primary RT (n=18). They showed a significant increase in the v_e and a decrease in the k_{ep}. The K^{trans} increased; however, the difference did not reach significance [90,91].

We evaluated thirty-six patients with oral cancer before and after preoperative CRT. In spite of the very low radiation dose administered in the PGs, both the ΔK^{trans} and Δv_e linearly correlated with the mean dose. We concluded that CRT caused a loss of the acinar cells, which then resulted in an increase in the percentage of the EES. The low radiation dose administered in this study may have caused an early vascular response, which typically involves a phase of vasodilatation and an increase in blood supply.

DISCUSSION AND CONCLUSION

The early reports of DWI generally showed that the most malignant tumors have a lower ADC compared to benign lesions. A large increase in the ADC during treatment or in the early post-treatment period was suggestive of a good response to the treatment, and a small increase or decrease was suggestive of treatment failure. Care should be taken when translating these published data into clinical practice, because various artifacts are associated with DW-SS-EPI.

The TK model analysis has the potential to predict and monitoring the tumor response to treatment. It also has potential for evaluating the function of the salivary gland. However, the parameters reported in the literature vary considerably; therefore, it is difficult to compare the values of the parameters among research groups. The establishment of a method for the accurate AIF measurement and accurate T_1 mapping, and a standardized pharmacokinetic model are needed for the wider application of this technique in clinical practice.

Both DWI and the pharmacokinetic analysis of the DCE-MRI have shown a wide range of potential benefits in the head and neck region, but more comparative studies with established scan techniques and the quantification of the data are required.

ACKNOWLEDGEMENT

This work was supported by an MEXT (Ministry of Education, Culture, Sports, Science and Technology) Grant-in-Aid for Scientific Research (C) 2 4 5 9 2 8 3 4.

REFERENCES

1. Schaefer PW, Grant PE, Gonzalez RG. Diffusion-weighted MR imaging of the brain. Radiology. 2000; 217: 331-345.
2. Buckley BT, Wainwright A, Meagher T, Briley D. Audit of a policy of magnetic resonance imaging with diffusion-weighted imaging as first-line neuroimaging for in-patients with clinically suspected acute stroke. Clin Radiol. 2003; 58: 234-237.
3. Thoeny HC, De Keyzer F, King AD. Diffusion-weighted MR imaging in the head and neck. Radiology. 2012; 263: 19-32.
4. Chawla S, Kim S, Wang S, Poptani H. Diffusion-weighted imaging in head and neck cancers. Future Oncol. 2009; 5: 959-975.
5. Tofts PS. Modeling tracer kinetics in dynamic Gd-DTPA MR imaging. J Magn Reson Imaging. 1997; 7: 91-101.
6. Tofts PS, Brix G, Buckley DL, Evelhoch JL, Henderson E, Knopp MV, et al. Estimating kinetic parameters from dynamic contrast-enhanced T(1)-weighted MRI of a diffusable tracer: standardized quantities and symbols. J Magn Reson Imaging. 1999; 10: 223-232.
7. Leach MO, Morgan B, Tofts PS, Buckley DL, Huang W, Horsfield MA, et al. Experimental Cancer Medicine Centres Imaging Network Steering Committee. Imaging vascular function for early stage clinical trials using dynamic contrast-enhanced magnetic resonance imaging. Eur Radiol. 2012; 22: 1451-1464.
8. Zwick S, Brix G, Tofts PS, Strecker R, Kopp-Schneider A, Laue H, et al. Simulation-based comparison of two approaches frequently used for dynamic contrast-enhanced MRI. Eur Radiol. 2010; 20: 432-442.
9. Stejskal EO, Tanner J. Spin diffusion measurements: spin echoes in the presence of a time-dependent field gradient. J Chem Phys. 1965; 42: 288-292.
10. Bammer R. Basic principles of diffusion-weighted imaging. Eur J Radiol. 2003; 45: 169-184.
11. Basser PJ. Inferring microstructural features and the physiological state of tissues from diffusion-weighted images. NMR Biomed. 1995; 8: 333-344.
12. Mori S, van Zijl PC. Diffusion weighting by the trace of the diffusion tensor within a single scan. Magn Reson Med. 1995; 33: 41-52.
13. Hennel F. Image-based reduction of artifacts in multishot echo-planar imaging. J Magn Reson. 1998; 134: 206-213.
14. Skare S, Newbould RD, Clayton DB, Albers GW, Nagle S, Bammer R. Clinical multishot DW-EPI through parallel imaging with considerations of susceptibility, motion, and noise. Magn Reson Med. 2007; 57: 881-890.
15. Yamashita K, Yoshiura T, Hiwatashi A, Kamano H, Dashjamts T, Shibata S, et al. Detection of middle ear cholesteatoma by diffusion-weighted MR imaging: multishot echo-planar imaging compared with single-shot echo-planar imaging. AJNR Am J Neuroradiol. 2011; 32: 1915-1918.
16. Reese TG, Heid O, Weisskoff RM, Wedeen VJ. Reduction of eddy-current-induced distortion in diffusion MRI using a twice-refocused spin echo. Magn Reson Med. 2003; 49: 177-182.
17. Kyriazi S, Blackledge M, Collins DJ, Desouza NM. Optimising diffusion-weighted imaging in the abdomen and pelvis: comparison of image quality between monopolar and bipolar single-shot spin-echo echo-planar sequences. Eur Radiol. 2010; 20: 2422-2431.
18. Verhappen MH, Pouwels PJ, Ljumanovic R, van der Putten L, Knol DL, De Bree R, et al. Diffusion-weighted MR imaging in head and neck cancer: comparison between half-fourier acquired single-shot turbo spin-echo and EPI techniques. AJNR Am J Neuroradiol. 2012; 33: 1239-1246.
19. Sakamoto J, Sasaki Y, Otonari-Yamamoto M, Sano T. Comparison of various methods for quantification of apparent diffusion coefficient of head and neck lesions with HASTE diffusion-weighted MR imaging. Oral Surg Oral Med Oral Pathol Oral Radiol. 2012; 114: 266-276.
20. Sakamoto J, Yoshino N, Okochi K, Imaizumi A, Tetsumura A, Kurohara K, et al. Tissue characterization of head and neck lesions using

diffusion-weighted MR imaging with SPLICE. Eur J Radiol. 2009; 69: 260-268.

21. Yoshino N, Yamada I, Ohbayashi N, Honda E, Ida M, Kurabayashi T, et al. Salivary glands and lesions: evaluation of apparent diffusion coefficients with split-echo diffusion-weighted MR imaging--initial results. Radiology. 2001; 221: 837-842.
22. Liu C, Moseley ME, Bammer R. Simultaneous phase correction and SENSE reconstruction for navigated multi-shot DWI with non-cartesian k-space sampling. Magn Reson Med. 2005; 54: 1412-1422.
23. Chen X, Xian J, Wang X, Wang Y, Zhang Z, Guo J, et al. Role of periodically rotated overlapping parallel lines with enhanced reconstruction diffusion-weighted imaging in correcting distortion and evaluating head and neck masses using 3 T MRI. Clin Radiol. 2013.
24. Wang J, Takashima S, Takayama F, Kawakami S, Saito A, Matsushita T, et al. Head and neck lesions: characterization with diffusion-weighted echo-planar MR imaging. Radiology. 2001; 220: 621-630.
25. Srinivasan A, Dvorak R, Perni K, Rohrer S, Mukherji SK. Differentiation of benign and malignant pathology in the head and neck using 3T apparent diffusion coefficient values: early experience. AJNR Am J Neuroradiol. 2008; 29: 40-44.
26. Eida S, Sumi M, Sakihama N, Takahashi H, Nakamura T. Apparent diffusion coefficient mapping of salivary gland tumors: prediction of the benignancy and malignancy. AJNR Am J Neuroradiol. 2007; 28: 116-121.
27. Habermann CR, Arndt C, Graessner J, Diestel L, Petersen KU, Reitmeier F, et al. Diffusion-weighted echo-planar MR imaging of primary parotid gland tumors: is a prediction of different histologic subtypes possible? AJNR Am J Neuroradiol. 2009; 30: 591-596.
28. Habermann CR, Gossrau P, Graessner J, Arndt C, Cramer MC, Reitmeier F, et al. Diffusion-weighted echo-planar MRI: a valuable tool for differentiating primary parotid gland tumors? Rofo. 2005; 177: 940-945.
29. Yabuuchi H, Matsuo Y, Kamitani T, Setoguchi T, Okafuji T, Soeda H, et al. Parotid gland tumors: can addition of diffusion-weighted MR imaging to dynamic contrast-enhanced MR imaging improve diagnostic accuracy in characterization? Radiology. 2008; 249: 909-916.
30. Holzapfel K, Duetsch S, Fauser C, Eiber M, Rummeny EJ, Gaa J. Value of diffusion-weighted MR imaging in the differentiation between benign and malignant cervical lymph nodes. Eur J Radiol. 2009; 72: 381-387.
31. de Bondt RB, Hoeberigs MC, Nelemans PJ, Deserno WM, Peutz-Kootstra C, Kremer B, et al. Diagnostic accuracy and additional value of diffusion-weighted imaging for discrimination of malignant cervical lymph nodes in head and neck squamous cell carcinoma. Neuroradiology. 2009; 51: 183-192.
32. Vandecaveye V, De Keyzer F, Hermans R. Diffusion-weighted magnetic resonance imaging in neck lymph adenopathy. Cancer Imaging. 2008; 8: 173-180.
33. Sumi M, Sakihama N, Sumi T, Morikawa M, Uetani M, Kabasawa H, et al. Discrimination of metastatic cervical lymph nodes with diffusion-weighted MR imaging in patients with head and neck cancer. AJNR Am J Neuroradiol. 2003; 24: 1627-1634.
34. Zhang Y, Chen J, Shen J, Zhong J, Ye R, Liang B. Apparent diffusion coefficient values of necrotic and solid portion of lymph nodes: differential diagnostic value in cervical lymphadenopathy. Clin Radiol. 2013; 68: 224-231.
35. Park JK, Kim SE, Trieman GS, Parker D, Jeong EK. High-resolution diffusion-weighted imaging of neck lymph nodes using 2D-single-shot interleaved multiple inner volume imaging diffusion-weighted echo-planar imaging at 3T. AJNR Am J Neuroradiol. 2011; 32: 1173-1177.
36. Hatakenaka M, Nakamura K, Yabuuchi H, Shioyama Y, Matsuo Y, Ohnishi K, et al. Pretreatment apparent diffusion coefficient of the primary lesion correlates with local failure in head-and-neck cancer treated with chemoradiotherapy or radiotherapy. Int J Radiat Oncol Biol Phys. 2011; 81: 339-345.
37. Ohnishi K, Shioyama Y, Hatakenaka M, Nakamura K, Abe K, Yoshiura T, et al. Prediction of local failures with a combination of pretreatment tumor volume and apparent diffusion coefficient in patients treated with definitive radiotherapy for hypopharyngeal or oropharyngeal squamous cell carcinoma. J Radiat Res. 2011; 52: 522-530.
38. Kim S, Loevner L, Quon H, Sherman E, Weinstein G, Kilger A, et al. Diffusion-weighted magnetic resonance imaging for predicting and detecting early response to chemoradiation therapy of squamous cell carcinomas of the head and neck. Clin Cancer Res. 2009; 15: 986-994.
39. Chawla S, Kim S, Dougherty L, Wang S, Loevner LA, Quon H, et al. Pretreatment diffusion-weighted and dynamic contrast-enhanced MRI for prediction of local treatment response in squamous cell carcinomas of the head and neck. AJR Am J Roentgenol. 2013; 200: 35-43.
40. Vandecaveye V, De Keyzer F, Dirix P, Lambrecht M, Nuyts S, Hermans R. Applications of diffusion-weighted magnetic resonance imaging in head and neck squamous cell carcinoma. Neuroradiology. 2010; 52: 773-784.
41. King AD, Mo FK, Yu KH, Yeung DK, Zhou H, Bhatia KS, et al. Squamous cell carcinoma of the head and neck: diffusion-weighted MR imaging for prediction and monitoring of treatment response. Eur Radiol. 2010; 20: 2213-2220.
42. Vandecaveye V, Dirix P, De Keyzer F, de Beeck KO, Vander Poorten V, Roebben I, et al. Predictive value of diffusion-weighted magnetic resonance imaging during chemoradiotherapy for head and neck squamous cell carcinoma. Eur Radiol. 2010; 20: 1703-1714.
43. Afaq A, Andreou A, Koh DM. Diffusion-weighted magnetic resonance imaging for tumour response assessment: why, when and how? Cancer Imaging. 2010; 10 Spec no A: S179-188.
44. Berrak S, Chawla S, Kim S, Quon H, Sherman E, Loevner LA, et al. Diffusion weighted imaging in predicting progression free survival in patients with squamous cell carcinomas of the head and neck treated with induction chemotherapy. Acad Radiol. 2011; 18: 1225-1232.
45. Shimosato Y, Obosh S, Baba K, Histologicalevaluation of effects of radiotherapy and chemotherapy for carcinomas. Japanese Journal of Clinical Oncology.1971; 1: 19-35.
46. Mori S, Crain BJ, Chacko VP, van Zijl PC. Three-dimensional tracking of axonal projections in the brain by magnetic resonance imaging. Ann Neurol. 1999; 45: 265-269.
47. Damon BM, Ding Z, Anderson AW, Freyer AS, Gore JC. Validation of diffusion tensor MRI-based muscle fiber tracking. Magn Reson Med. 2002; 48: 97-104.
48. Hodaie M, Chen DQ, Quan J, Laperriere N. Tractography delineates microstructural changes in the trigeminal nerve after focal radiosurgery for trigeminal neuralgia. PLoS One. 2012; 7: e32745.
49. Taoka T, Hirabayashi H, Nakagawa H, Sakamoto M, Myochin K, Hirohashi S, et al. Displacement of the facial nerve course by vestibular schwannoma: preoperative visualization using diffusion tensor tractography. J Magn Reson Imaging. 2006; 24: 1005-1010.
50. Mori S, Kaneda T, Fujita Y, Kato M, Sakayanagi M, Minami M. Diffusion tensor tractography for the inferior alveolar nerve (V3): initial experiment. Oral Surg Oral Med Oral Pathol Oral Radiol Endod. 2008; 106: 270-274.
51. Akter M, Hirai T, Minoda R, Murakami R, Saiki S, Okuaki T, et al.

Diffusion tensor tractography in the head-and-neck region using a clinical 3-T MR scanner. Acad Radiol. 2009; 16: 858-865.

52. Tseng WY, Wedeen VJ, Reese TG, Smith RN, Halpern EF. Diffusion tensor MRI of myocardial fibers and sheets: correspondence with visible cut-face texture. J Magn Reson Imaging. 2003; 17: 31-42.

53. Galbán CJ, Maderwald S, Uffmann K, de Greiff A, Ladd ME. Diffusive sensitivity to muscle architecture: a magnetic resonance diffusion tensor imaging study of the human calf. Eur J Appl Physiol. 2004; 93: 253-262.

54. Shiraishi T, Chikui T, Yoshiura K, Yuasa K. Evaluation of T2 values and apparent diffusion coefficient of the masseter muscle by clenching. Dentomaxillofac Radiol. 2011; 40: 35-41.

55. Chikui T, Shiraishi T, Ichihara T, Kawazu T, Hatakenaka M, Kami Y, et al. Effect of clenching on T2 and diffusion parameters of the masseter muscle. Acta Radiol. 2010; 51: 58-63.

56. Hatakenaka M, Yabuuchi H, Matsuo Y, Okafuji T, Kamitani T, Setoguchi T, et al. Effect of passive muscle length change on apparent diffusion coefficient: detection with clinical MR imaging. Magn Reson Med Sci. 2008; 7: 59-63.

57. Hatakenaka M, Matsuo Y, Setoguchi T, Yabuuchi H, Okafuji T, Kamitani T, et al. Alteration of proton diffusivity associated with passive muscle extension and contraction. J Magn Reson Imaging. 2008; 27: 932-937.

58. Deux JF, Malzy P, Paragios N, Bassez G, Luciani A, Zerbib P, et al. Assessment of calf muscle contraction by diffusion tensor imaging. Eur Radiol. 2008; 18: 2303-2310.

59. Collins DJ, Padhani AR. Dynamic magnetic resonance imaging of tumor perfusion. Approaches and biomedical challenges. IEEE Eng Med Biol Mag. 2004; 23: 65-83.

60. Asaumi J, Yanagi Y, Hisatomi M, Matsuzaki H, Konouchi H, Kishi K. The value of dynamic contrast-enhanced MRI in diagnosis of malignant lymphoma of the head and neck. Eur J Radiol. 2003; 48: 183-187.

61. Asaumi J, Yanagi Y, Konouchi H, Hisatomi M, Matsuzaki H, Kishi K. Application of dynamic contrast-enhanced MRI to differentiate malignant lymphoma from squamous cell carcinoma in the head and neck. Oral Oncol. 2004; 40: 579-584.

62. Yabuuchi H, Fukuya T, Tajima T, Hachitanda Y, Tomita K, Koga M. Salivary gland tumors: diagnostic value of gadolinium-enhanced dynamic MR imaging with histopathologic correlation. Radiology. 2003; 226: 345-354.

63. Hisatomi M, Asaumi J, Yanagi Y, Konouchi H, Matsuzaki H, Honda Y, et al. Assessment of pleomorphic adenomas using MRI and dynamic contrast enhanced MRI. Oral Oncol. 2003; 39: 574-579.

64. Eida S, Ohki M, Sumi M, Yamada T, Nakamura T. MR factor analysis: improved technology for the assessment of 2D dynamic structures of benign and malignant salivary gland tumors. J Magn Reson Imaging. 2008; 27: 1256-1262.

65. Brix G, Semmler W, Port R, Schad LR, Layer G, Lorenz WJ. Pharmacokinetic parameters in CNS Gd-DTPA enhanced MR imaging. J Comput Assist Tomogr. 1991; 15: 621-628.

66. Parker GJ, Suckling J, Tanner SF, Padhani AR, Revell PB, Husband JE, et al. Probing tumor microvascularity by measurement, analysis and display of contrast agent uptake kinetics. J Magn Reson Imaging. 1997; 7: 564-574.

67. Fritz-Hansen T, Rostrup E, Larsson HB, Søndergaard L, Ring P, Henriksen O. Measurement of the arterial concentration of Gd-DTPA using MRI: a step toward quantitative perfusion imaging. Magn Reson Med. 1996; 36: 225-231.

68. Crone c. The permeability of capillaries in various organs as determined by use of the 'indicator diffusion' method. Acta physiol scand. 1963; 58: 292-305.

69. Meng R, Chang SD, Jones EC, Goldenberg SL, Kozlowski P. Comparison between population average and experimentally measured arterial input function in predicting biopsy results in prostate cancer. Acad Radiol. 2010; 17: 520-525.

70. Akbudak E, Conturo TE. Arterial input functions from MR phase imaging. Magn Reson Med. 1996; 36: 809-815.

71. Cron GO, Foottit C, Yankeelov TE, Avruch LI, Schweitzer ME, Cameron I. Arterial input functions determined from MR signal magnitude and phase for quantitative dynamic contrast-enhanced MRI in the human pelvis. Magn Reson Med. 2011; 66: 498-504.

72. Korporaal JG, van den Berg CA, van Osch MJ, Groenendaal G, van Vulpen M, van der Heide UA. Phase-based arterial input function measurements in the femoral arteries for quantification of dynamic contrast-enhanced (DCE) MRI and comparison with DCE-CT. Magn Reson Med. 2011; 66: 1267-1274.

73. Parker GJ, Roberts C, Macdonald A, Buonaccorsi GA, Cheung S, Buckley DL, et al. Experimentally-derived functional form for a population-averaged high-temporal-resolution arterial input function for dynamic contrast-enhanced MRI. Magn Reson Med. 2006; 56: 993-1000.

74. Weinmann HJ, Laniado M, Mützel W. Pharmacokinetics of GdDTPA/dimeglumine after intravenous injection into healthy volunteers. Physiol Chem Phys Med NMR. 1984; 16: 167-172.

75. Wang HZ, Riederer SJ, Lee JN. Optimizing the precision in T1 relaxation estimation using limited flip angles. Magn Reson Med. 1987; 5: 399-416.

76. Yuan J, Chow SK, Yeung DK, Ahuja AT, King AD. Quantitative evaluation of dual-flip-angle T1 mapping on DCE-MRI kinetic parameter estimation in head and neck. Quant Imaging Med Surg. 2012; 2: 245-253.

77. Manuel A, Li W, Jellus V, Hughes T, Prasad PV. Variable flip angle-based fast three-dimensional T1 mapping for delayed gadolinium-enhanced MRI of cartilage of the knee: need for B1 correction. Magn Reson Med. 2011; 65: 1377-1383.

78. Andreisek G, White LM, Yang Y, Robinson E, Cheng HL, Sussman MS. Delayed gadolinium-enhanced MR imaging of articular cartilage: three-dimensional T1 mapping with variable flip angles and B1 correction. Radiology. 2009; 252: 865-873.

79. Lee FK, King AD, Ma BB, Yeung DK. Dynamic contrast enhancement magnetic resonance imaging (DCE-MRI) for differential diagnosis in head and neck cancers. Eur J Radiol. 2012; 81: 784-788.

80. Van Cann EM, Rijpkema M, Heerschap A, van der Bilt A, Koole R, Stoelinga PJ. Quantitative dynamic contrast-enhanced MRI for the assessment of mandibular invasion by squamous cell carcinoma. Oral Oncol. 2008; 44: 1147-1154.

81. Jansen JF, Koutcher JA, Shukla-Dave A. Non-invasive imaging of angiogenesis in head and neck squamous cell carcinoma. Angiogenesis. 2010; 13: 149-160.

82. Cao Y, Popovtzer A, Li D, Chepeha DB, Moyer JS, Prince ME, et al. Early prediction of outcome in advanced head-and-neck cancer based on tumor blood volume alterations during therapy: a prospective study. Int J Radiat Oncol Biol Phys. 2008; 72: 1287-1290.

83. Shukla-Dave A, Lee NY, Jansen JF, Thaler HT, Stambuk HE, Fury MG, et al. Dynamic contrast-enhanced magnetic resonance imaging as a predictor of outcome in head-and-neck squamous cell carcinoma patients with nodal metastases. Int J Radiat Oncol Biol Phys. 2012; 82: 1837-1844.

84. Kim S, Loevner LA, Quon H, Kilger A, Sherman E, Weinstein G, et al. Prediction of response to chemoradiation therapy in squamous cell carcinomas of the head and neck using dynamic contrast-enhanced MR imaging. AJNR Am J Neuroradiol. 2010; 31: 262-268.

85. Hoskin PJ, Saunders MI, Goodchild K, Powell ME, Taylor NJ, Baddeley H. Dynamic contrast enhanced magnetic resonance scanning as a predictor of response to accelerated radiotherapy for advanced head and neck cancer. Br J Radiol. 1999; 72: 1093-1098.

86. Chikui T, Kawano S, Kawazu T, Hatakenaka M, Koga S, Ohga M, et al. Prediction and monitoring of the response to chemoradiotherapy in oral squamous cell carcinomas using a pharmacokinetic analysis based on the dynamic contrast-enhanced MR imaging findings. Eur Radiol. 2011; 21: 1699-1708.

87. Chikui T, Kitamoto E, Kawano S, Sugiura T, Obara M, Simonetti AW, et al. Pharmacokinetic analysis based on dynamic contrast-enhanced MRI for evaluating tumor response to preoperative therapy for oral cancer. J Magn Reson Imaging. 2012; 36: 589-597.

88. Oberholzer K, Pohlmann A, Schreiber W, Mildenberger P, Kunz P, Schmidberger H, et al. Assessment of tumor microcirculation with dynamic contrast-enhanced MRI in patients with esophageal cancer: initial experience. J Magn Reson Imaging. 2008; 27: 1296-1301.

89. Roberts C, Parker GJ, Rose CJ, Watson Y, O'Connor JP, Stivaros SM, et al. Glandular function in Sjögren syndrome: assessment with dynamic contrast-enhanced MR imaging and tracer kinetic modeling--initial experience. Radiology. 2008; 246: 845-853.

90. Houweling AC, Schakel T, van den Berg CA, Philippens ME, Roesink JM, Terhaard CH, et al. MRI to quantify early radiation-induced changes in the salivary glands. Radiother Oncol. 2011; 100: 386-389.

91. Lee FK, King AD, Kam MK, Ma BB, Yeung DK. Radiation injury of the parotid glands during treatment for head and neck cancer: assessment using dynamic contrast-enhanced MR imaging. Radiat Res. 2011; 175: 291-296.

Cite this article

Chikui T, Ohga M, Kitamoto E, Shiraishi T, Kawano S, et al. (2014) Quantification of Diffusion and Permeability of MRI in the Head and Neck Region. J Radiol Radiat Ther 2(2): 1047.